

# Novel CMOS-Compatible Mo–AlN–Mo Platform for Metamaterial-Based Mid-IR Absorber

Dihan Hasan,<sup>†,‡,§</sup> Prakash Pitchappa,<sup>†,‡,§</sup> Jiahui Wang,<sup>†,‡,§</sup> Tao Wang,<sup>†,‡</sup> Bin Yang,<sup>||</sup> Chong Pei Ho,<sup>†,‡,§</sup> and Chengkuo Lee<sup>\*,†,‡,§,⊥</sup>

<sup>†</sup>Department of Electrical & Computer Engineering, National University of Singapore, 4 Engineering Drive 3, 117576, Singapore

<sup>||</sup>Department of Micro/Nano Electronics, Shanghai Jiao Tong University, Dong Chuan Road 800, 200240 Shanghai, People's Republic of China

<sup>‡</sup>NUS Suzhou Research Institute (NUSRI), Suzhou Industrial Park, Suzhou, People's Republic of China 215123

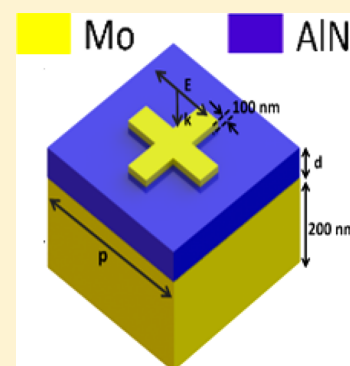
<sup>§</sup>Center for Intelligent Sensors and MEMS, National University of Singapore, 4 Engineering Drive 3, Singapore 117576

<sup>⊥</sup>Graduate School for Integrative Science and Engineering, National University of Singapore, Singapore

## Supporting Information

**ABSTRACT:** We demonstrate a new CMOS compatible metal–dielectric–metal (Mo–AlN–Mo) platform of metamaterial absorber for refractory and narrowband applications at mid-IR. Comparison with the recently reported CMOS compatible plasmonic TiN shows superior reflectivity of Mo thin film at mid-IR wavelengths (3–8  $\mu\text{m}$ ), while AlN provides large thermal stability and thermal conductivity, mid- to far-IR transparency and both second and third order nonlinear effect and satisfies the matching condition of thermal expansion coefficient with Mo toward minimizing the thermal stress. We demonstrate the proof-of-concept of reducing the thermal stress up to 400° by considering a high stress, CMOS platform of SiO<sub>2</sub>. We further report temporal measurement of the resonance intensity and wavelength-shift of the absorber structures and confirm the robust performance of the platform over prolonged heating. Finally, we propose a method to perform surface enhanced infrared absorption (SEIRA) spectroscopy of biological samples demanding biocompatibility on the massively scalable CMOS platform and demonstrate strong coupling to the amide vibrational bonds of silk fibroin at mid-IR. We envisage the proposed platform will be a versatile avenue for thermophotovoltaic energy conversion and emission at low thermal stress, fast thermal detection, and large scale, low form factor, and integrated sensors with the ubiquitous CMOS technology.

**KEYWORDS:** AlN, CMOS, mid-IR, refractory, SEIRA thermal stress, thermal detection



Metamaterial-based optical structures referring to engineered material with properties not readily available in nature, are finding a multitude of applications in sensing,<sup>1</sup> solar, and thermophotovoltaic energy conversion,<sup>2,3</sup> optical communication,<sup>4</sup> big data storage,<sup>5</sup> and all-optical computation.<sup>6</sup> Designer surface plasmons, commonly known as collective electron oscillations in periodic, subwavelength structures made of metal provide a large degree of freedom for realizing the aforementioned applications in a broad wavelength range starting from the visible to microwave spectrum due to their dispersion.<sup>7–14</sup> Thanks to the pioneering role of nanotechnology, complicated plasmonic architectures with multifunctionalities have been already demonstrated.<sup>15–26</sup> However, large-scale application of plasmonic metamaterial is strongly dependent on both the scalability and repeatability of the fabrication process, which can be reasonably ensured in CMOS technology. Very recently, CMOS fabricated designer optical structures have been reported to achieve high-Q Fabry–Pérot (FP) resonance for gas sensing,<sup>27,28</sup> MEMS tunable metamaterials for terahertz communication,<sup>29,30</sup> and switchable mid-IR absorber,<sup>31</sup> while relying on a fairly challenging process flow. On the other hand,

refractory plasmonics is an emerging niche, especially in photothermal therapy,<sup>32</sup> heat-assisted magnetic recording (HAMR),<sup>33</sup> and thermophotovoltaic energy conversion<sup>34</sup> deploying refractory material with chemical stability at temperatures at and above 2000 °C in the design. In particular, metamaterial absorber offers ultraminiaturization, wide adaptability, and increased effectiveness for energy-efficient emitters, sensitive photodetectors, wireless communication, and solar and thermophotovoltaics.<sup>35–41</sup>

Although refractory broadband solar absorber based on CMOS compatible TiN have been demonstrated,<sup>36</sup> narrowband design based on this platform still requires careful consideration of mechanical properties of the material interfaces. More importantly, mid-IR (3–8  $\mu\text{m}$ ) optical properties of TiN are yet to be explored for its applications in this wavelength range. On the contrary, a non-CMOS combination of Pt–Al<sub>2</sub>O<sub>3</sub> with minimal thermal expansion coefficient (TEC) mismatch is considered by Padilla and co-workers.<sup>37</sup> Simultaneously, it is also

Received: September 6, 2016

Published: January 17, 2017

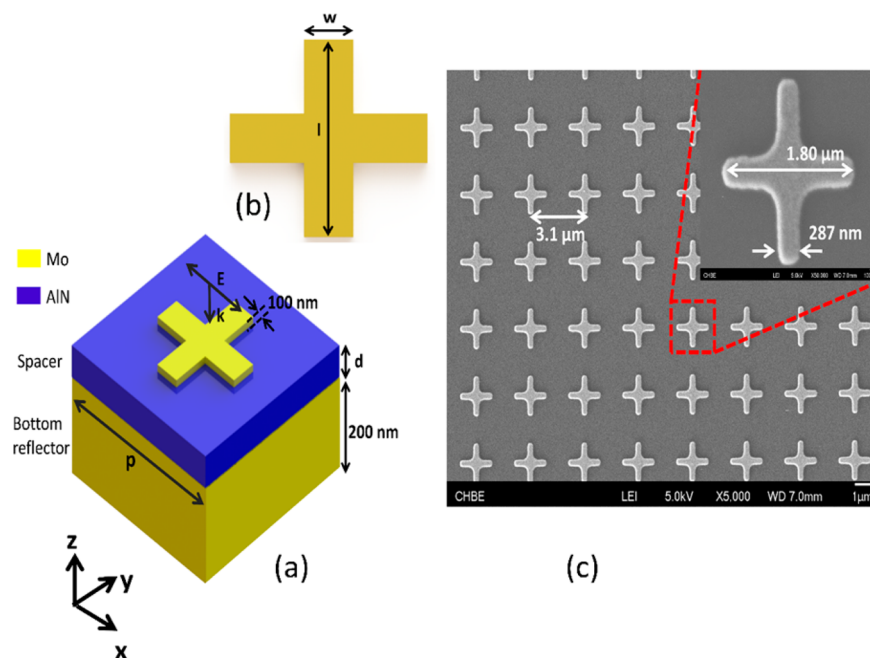


**Figure 1.** (a) 3D schematic of Mo–AlN–Mo absorber. (b) 2D layout of the metamaterial pattern. (c) FESEM image of the array of metamaterial patterns. Inset: zoomed-in SEM image of the unit cell. For comparison, we also replace the AlN spacer with SiO<sub>2</sub> spacer of similar thickness.

**Table 1. Comparison of Different Metals for Metamaterial Structures**

metal	melting point (°C)	electrical conductivity ( $\times 10^7$ S/m @ 20 °C)	plasma frequency ( $\times 10^{15}$ Hz)	coefficient of thermal expansion: CTE ( $\times 10^{-6}$ K <sup>-1</sup> )	Young's modulus ( $E$ ; GPa)	CMOS compatibility
aluminum	660	3.5	3.57	24	70	yes
gold	1000	4.52	2.2	14	78	no
platinum	1770	0.944	1.25	8.8	168	no
TiN	2930	0.87	1.84	9.35	251	yes
molybdenum	2620	1.9	1.8	4.8	329	yes

**Table 2. Comparison of Mechanical Properties of the Spacer Material**

material	melting point (°C)	Young's modulus ( $E$ ; GPa)	Poisson ratio ( $\mu$ )	CTE ( $\times 10^{-6}$ K <sup>-1</sup> )	thermal conductivity (W/m·K)
aluminum nitride	2200	344.8	0.287	4.6	285
SiO <sub>2</sub>	1600	70	0.17	0.5	1.4
aluminum oxide	2072	353.1	0.22	4.5	25.08

essential to preserve large thermal conductivity of the design for fast thermal response in high speed applications, that is, mid-IR spectral imaging.<sup>38</sup> With such key requirements under consideration, here, we propose a fully CMOS combination of Mo–AlN–Mo metamaterial-based mid-IR absorber structures. It is also expected to achieve advanced electromagnetic properties, for example, near unity absorption across multibands by judicious design on the CMOS platform.<sup>45</sup>

The robust performance of the proposed platform with minimal thermal stress is further explored under different heating conditions. Our mid-IR investigation shows higher reflectivity of Mo thin film than TiN film and broadband transparency of AlN, enabling the design of highly scalable, large contrast and narrowband structures. The large thermal conductivity of AlN ( $\sim 285$  W/m·K) can be leveraged further to ensure the fast thermal response of the designed structures. The low thermal stress also enables the platform to be deployed as a spectrally selective emitter operating at high temperature in fully integrated surface enhanced infrared absorption (SEIRA) sensors for biochemicals and gases in the mid-IR spectrum.<sup>40</sup> It is

worthwhile to note that recently reported CMOS compatible SEIRA platforms lack the required refractory property to be deployed as a durable energy efficient emitter.<sup>41,42</sup> An added advantage of AlN is it offers both the second and the third order nonlinear effects providing a route for on-chip up-conversion of mid-IR spectral fingerprints into shorter wavelengths for imaging and interpretation.<sup>43</sup> As a preliminary study, here we report strong geometry dependent coupling of mid-IR absorption lines into the structures modified to allow a wide range of surface functionalization. The coupling effect is suggestive of the sensitivity of the proposed CMOS compatible platform as found in their non-CMOS, noble metal (Au) counterparts.

#### Design Details, Fabrication, and Characterization.

Figure 1a shows the 3D schematic of the cross wire, metal-dielectric-metal absorber structure. Here, the periodicity ( $p$ ), thickness of the top metal layer, and thickness of the back reflector are fixed at  $3.1 \mu\text{m}$ ,  $100 \text{ nm}$ , and  $200 \text{ nm}$ , respectively. The incident polarization is assumed to be along  $x$ -axis in simulation. Figure 1b shows the polarization-independent 2D layout of the structure, where  $w$  is the width and  $l$  is the length of

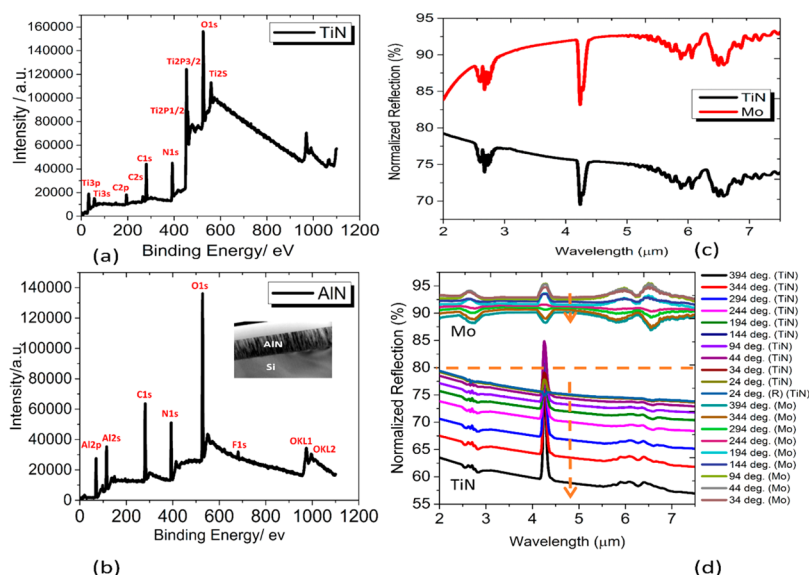


**Figure 2.** (a) X-ray photoelectron spectroscopy (XPS) of 30 nm TiN thin film obtained by atomic layer deposition (ALD) on Si substrate (b) XPS spectroscopy of 200 nm AlN on Mo reflector. Inset: TEM image of the film cross section on silicon substrate. (c) Comparison of reflection intensity between TiN and Mo on Si substrate. (d) Comparison between TiN and Mo reflection on intrinsic Si substrate under different temperatures. (R) represents the reverse cycle during which the sample is cooled down.

the pattern. In this experiment, we vary the spacer thickness and the pattern length. Figure 1c shows the field emission SEM (FESEM) image of the fabricated structure. In Table 1, a comparison of Mo with other CMOS and non-CMOS metal and TiN is provided, which clearly shows the strong refractory properties of Mo. Table 2 is the comparison of AlN with two other CMOS dielectrics, SiO<sub>2</sub> and Al<sub>2</sub>O<sub>3</sub>, which shows the large thermal conductivity and melting point of the nitride. A very good match of mechanical properties with that of Mo in Table 1 is easily discernible, which is essential for low stress operation of metamaterial absorber structure at high temperature. We consider the high stress SiO<sub>2</sub> platform for experimental comparison with the AlN platform in this work.

A bare 8" silicon wafer was cleaned and 200 nm of Mo followed by the AlN thin film for the spacer and the top Mo film for the patterns were sputtered deposited under high vacuum. For the case of SiO<sub>2</sub> platform, plasma enhanced chemical vapor deposition (PECVD) was performed. Deep UV photolithography process was used to define the metamaterial patterns. Finally, Mo was dry etched to form the final absorber structure. Figure 2a shows the X-ray photoelectron spectroscopy (XPS) of TiN film. The tin film was obtained by an optimized atomic layer deposition process using TiCl<sub>4</sub>/NH<sub>3</sub> chemistry. The roughness of the film is found to be around 0.5 nm. XPS peaks observed in the case of 200 nm AlN film on Mo reflector are shown in Figure 2b. For optical characterization, a broadband FTIR microscope integrated with a heat stage capable of heating up to 450° and controlled by a temperature regulator, is deployed. Figure 2c shows a large difference of reflectivity (~20%) between the Mo thin film and TiN thin film of similar thickness on Si substrate at the mid-IR spectrum. Note that, metallic properties of TiN strongly rely on its wavelength-dependent free carrier concentration.<sup>44</sup> From Table 1, it is clear that DC conductivity of TiN is at least 2 times less than in Mo. On the contrary, a comparison with Table 2 indicates large mechanical mismatch of TiN with the majority of the CMOS dielectrics applicable for scalable absorber design. The weaker reflection observed in ALD obtained TiN film can be possibly attributed to its reduced free

carrier interaction at mid-IR spectrum in comparison to its pure metallic Mo counterpart. Further improvement of reflection characteristics may require extensive investigation into the process dependent properties limiting its widespread application. Interestingly, no characteristic mid-IR peak is observed for this transition metal-nitride in the IR range of the experiment. On other hand, low wavenumber Raman study of the TiN film indeed reveals Ti–N vibrational peaks at (340, 540, and 950 cm<sup>-1</sup>) and, therefore, limits the broadband scalability of the TiN-based platform (Figure S1). Nevertheless, the weak reflection property of TiN can strongly reduce the overall quality factor and contrast of the narrowband resonance which are governed by the following equation as per the interference theory approximation,<sup>45</sup>

$$\tilde{r} = \tilde{r}_{12} - \frac{\tilde{t}_{12} \tilde{t}_{21} e^{i2\tilde{\beta}}}{1 + e^{i2\tilde{\beta}} \tilde{r}_{21}} \quad (1)$$

Here, the subscript 1 and 2 denote the air and metal medium, respectively.  $\tilde{r}$  and  $\tilde{t}$  are the complex reflection and transmission coefficient at the air–metal interface and  $\tilde{\beta}$  is the complex propagation constant in the dielectric spacer. Therefore, the absorption (A) defined as  $1 - |\tilde{r}|^2$  is strongly dominated by the reflectivity of the constituting metal layers. On the other hand, any stochastic interfacial damage can strongly perturb the infinitely summable interference condition and thereby weaken the quality of the absorption resonance. We further provide the temperature dependent reflection characteristic of TiN thin film and compare with that of Mo in Figure 2d. It is clear that TiN reflection is at least 15% less than in Mo. Moreover, we observe strongly dispersive nature of TiN in the mid-IR spectrum, which is attributed to wavelength dependence of the intraband electron transition of the metal nitride. The reduced reflection is correlated with the reduced dielectric contrast of TiN (Figure S2). The dispersive nature of TiN can be again confirmed from the transmission measurement of the thin film (Figure S3). The regular decrease of reflection intensity as the temperature increases is directly related to the increase of Drude damping

parameter due to electron scattering.<sup>46</sup> Such temperature dependent characteristic is also found to be strongly reversible. The experimental results in Figure 2c,d indicate that performance of narrowband metamaterial absorber structures based on TiN can be strongly affected at high temperature.

As a proof-of-concept, we provide the simulation results in near IR showing remarkably lower quality factor and resonance contrast of TiN design as compared to Mo design (Figure S4).

Figure 3a and b show the simulated and experimental absorption of the structure, respectively. Figure 3c shows the

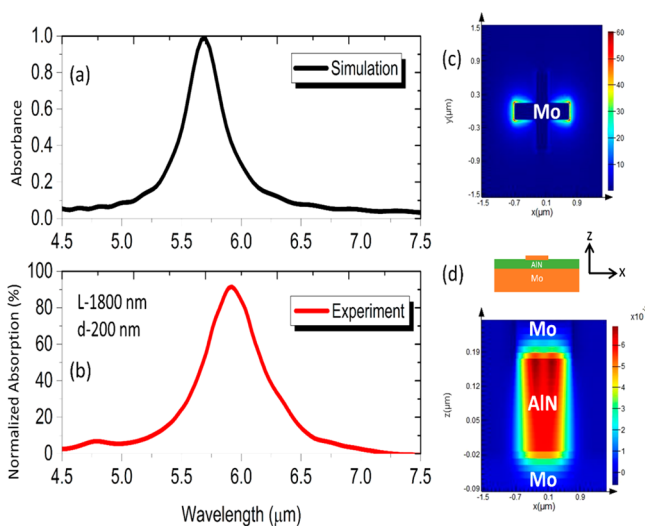


**Figure 3.** (a) Simulated absorption spectrum. (b) Experimental absorption spectrum. (c) Electric field distribution of the dipolar mode in the cross wire metamaterial pattern (period ( $p$ )  $3.1 \mu\text{m}$ , length ( $l$ )  $1800 \text{ nm}$ , width ( $w$ )  $283 \text{ nm}$ , spacer ( $d$ )  $200 \text{ nm}$ ). (d) H-field intensity distribution across the cross section of the absorber geometry in Figure 1a. The refractive index of AlN is assumed to be 2.00 and Drude model is considered for Mo permittivity.<sup>39</sup>

electric field distribution of the dipolar resonance. The magnetic field intensity in Figure 3d refers to strong near field coupling between the top metal pattern and the bottom metal reflector. The good agreement between the simulation and experimental result is suggestive of high quality and broadband transparency of AlN thin film on Mo reflector. Slight discrepancy between simulation and experimental result observed can be attributed to

fabrication induced imperfections, for example, corner roundness and optical dispersion of AlN. In this work, we geometrically vary the absorption resonance from 4 to  $8 \mu\text{m}$  without encountering any characteristic peak either from the metal layer or the spacer layer.

## RESULTS AND ANALYSIS

**Low Thermal Stress Characteristics. Symmetric Structure Analysis.** The stress ( $\sigma$ ) which is created by the heating process, mainly originates from two different sources as formulated in the following equations:<sup>47</sup>

$$\sigma = \sigma_{\text{th}} + \sigma_{\text{i}} \quad (2)$$

$$\sigma_{\text{th}} = \frac{E}{1 - \nu} \Delta\alpha \Delta T \quad (3)$$

$$\sigma_{\text{i}} = E\alpha\Delta T \quad (4)$$

Here,  $\sigma_{\text{th}}$  and  $\sigma_{\text{i}}$  are the residual and intrinsic stress, respectively.  $\Delta\alpha$ ,  $E$ ,  $\nu$ , and  $\Delta T$  are the thermal expansion coefficient (TCE) mismatch, Young's modulus, Poisson ratio, and temperature difference, respectively. Here,  $\sigma_{\text{th}}$  is the stress due to the TCE mismatch  $\Delta\alpha$  between the adjacent layers, whereas  $\sigma_{\text{i}}$  corresponds to stress due to the volumetric expansion of the respective layer when there is a positive temperature difference. From such a mechanical point of view, the combination of Mo and AlN has the least mismatch, while that of Mo and  $\text{SiO}_2$  has the highest mismatch. On the other hand, the refractive index of  $\text{SiO}_2$  is slightly smaller than that of AlN. Figure 4 is the proof-of-concept demonstration of the low stress Mo–AlN–Mo platform for metamaterial absorber consist of symmetric pattern. In each cycle, the temperature is systematically increased from 25 to  $400 \text{ }^\circ\text{C}$  in four steps and the absorption spectrum is recorded once a stable reading is achieved. The results in Figure 4a show the robustness of the AlN platform at high temperature with a negligible wavelength shift ( $\sim 25 \text{ nm}$ ) and intensity decrease ( $\sim 10\%$ ). Later, we discuss that such change is strongly reversible and mainly dominated by the conductivity decrease of the metal layers. On the contrary, the effect of increasing temperature on the resonance spectrum of  $\text{SiO}_2$  device is found to be more severe in Figure 4b. At  $400 \text{ }^\circ\text{C}$ , the  $\text{SiO}_2$  device is found to be significantly damaged with strongly dampened absorption resonance. Moreover, unwanted peaks coming from the carbon defects in PECVD  $\text{SiO}_2$  start to appear in the spectrum when the temperature reaches  $275 \text{ }^\circ\text{C}$ . Also note that, oxidation of Mo

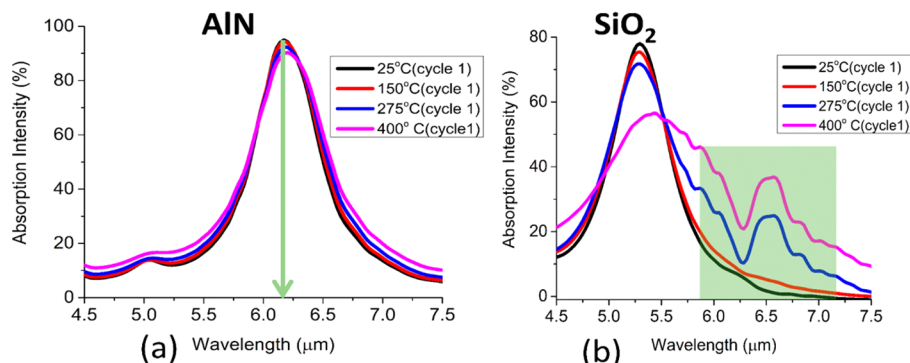


**Figure 4.** Proof-of-concept demonstration of low thermal stress absorber structure. (a) Mo–AlN–Mo configuration. (b) Mo– $\text{SiO}_2$ –Mo configuration. The length ( $l$ ), width ( $w$ ), and spacer ( $d$ ) are fixed at  $1900$ ,  $283$ , and  $200 \text{ nm}$ , respectively. The green arrow indicates the initial position of the resonance in the AlN device at room temperature. The transparent green rectangle refers to the unwanted peaks originating from carbon defect in PECVD oxide. The temperature-dependent measurement is taken 5 min after the heat stage is programmed, assuring the uniform heating of the sample.

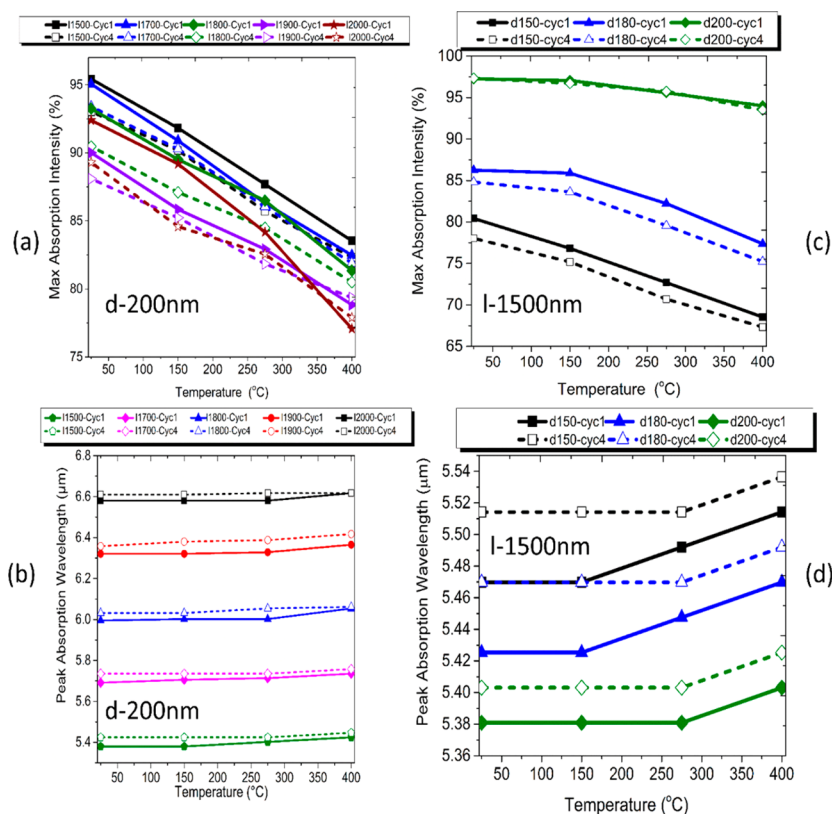


**Figure 5.** (a) Maximum absorption intensity versus temperature (a) at different lengths,  $l$ , while the spacer width,  $d$ , is fixed at 200 nm (c) at different spacer widths,  $d$ , while the length is fixed at 1500 nm. Peak absorption wavelength vs temperature (b) at different lengths,  $l$ , while the spacer width,  $d$ , is fixed at 200 nm (d) at different spacer widths:  $d$  while the length,  $l$ , is fixed at 1500 nm.

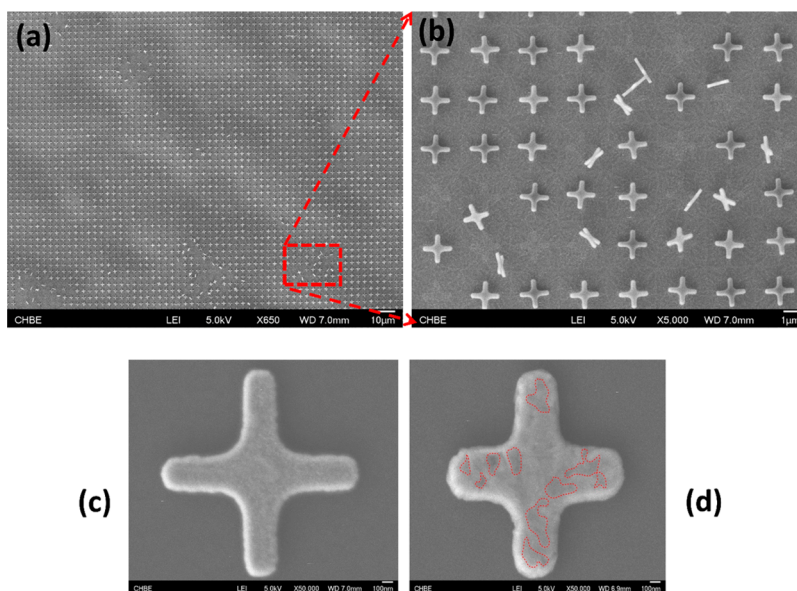


**Figure 6.** (a) FESEM image of the array of the patterns in Mo-SiO<sub>2</sub>-Mo configuration over an area of 100 by 65  $\mu\text{m}^2$  after annealing at 400° for 5 min over four cycles. (b) Zoomed in FESEM image of the annealed chip on SiO<sub>2</sub> platform. (c) FESEM image of the unit cell in Mo-AlN-Mo configuration after annealing at 400° for 5 min for four cycles. (d) FESEM image of the unit cell in Mo-SiO<sub>2</sub>-Mo configuration after annealing at 400° for 5 min for four cycles. Formation of random cracks is marked by the regions enclosed within the red dashed lines.

begins to occur at 1000 °C and beyond and, hence, can be ignored in our case.

In Figure 5, we compare the intensity variation and resonance shift between the first and fourth cycle of heating for a range of parameters:  $l$  and  $d$  of the AlN device. As observed, the overall

trend of both intensity variation and resonance shift over the four cycles is found to be preserved. Nevertheless, a net mismatch between the first and fourth cycle is still visible which implies the accumulated stress over the four cycles of heating. In general, the results are suggestive of repeatable and robust

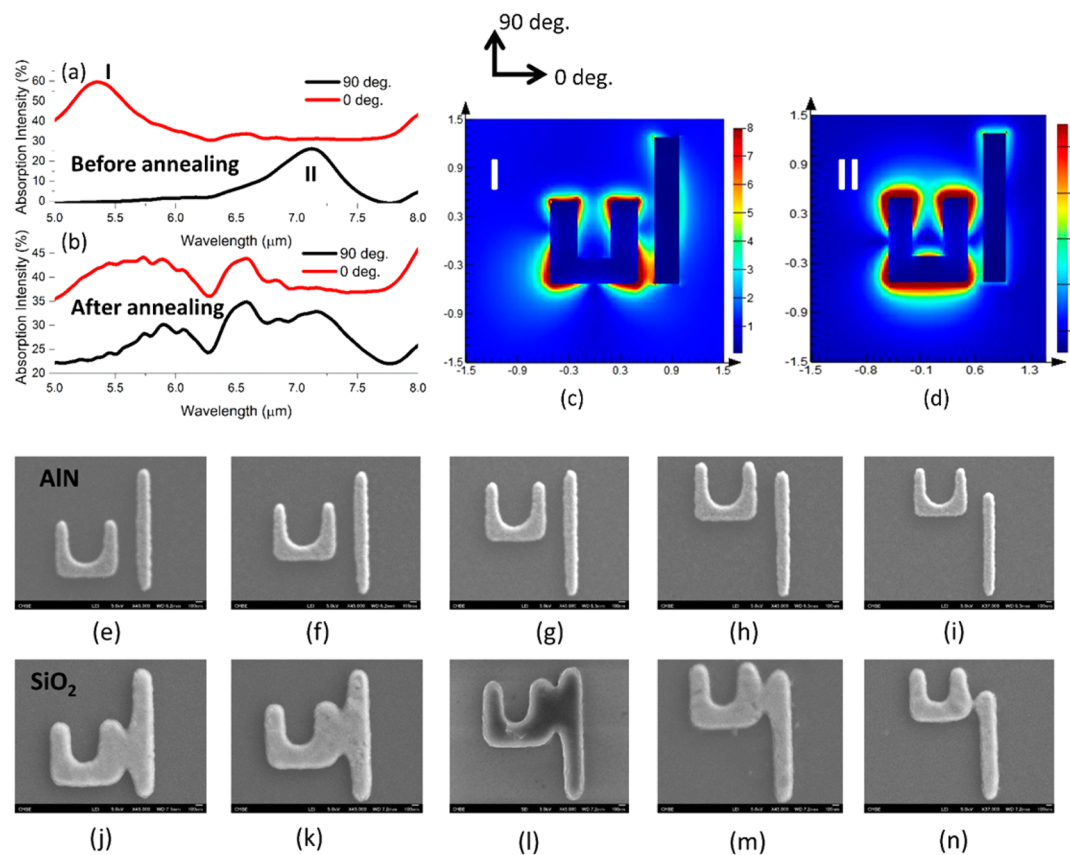


**Figure 7.** Polarization tuning experiment at 400°. (a) Polarization tuning before annealing and (b) after annealing in SiO<sub>2</sub> device. Origin of the resonance peaks (c) *E*-field distribution at spectral location I and (d) *E*-field distribution at location II. Effect of annealing on axis asymmetric structures designed for polarization tuning. (e–i) Metamaterial pattern on Mo–AlN–Mo configuration and (j–n) on Mo–SiO<sub>2</sub>–Mo configuration.

performance of the metamaterial platform as required for high temperature applications.

In Figure 6, FESEM image analysis of the chips subject to high temperature annealing is provided. Permanent damage of the SiO<sub>2</sub> device is observed in Figure 6a,b, whereas no such damage is observed in the case of AlN device. However, as seen, the permanent damage of the top metal patterns is highly localized. In fact, it is the interfacial damage between the dielectric spacer and the continuous back reflector that primarily affects the optical response of the whole array. The wavy nature of the topography in Figure 6a is corresponding to this. Such damage can strongly affect the multiple interference condition prescribed by eq 1 and ultimately deteriorates the quality factor and contrast of the absorption resonance. We further provide the experimental results which indicate the dominant effects of interfacial damage between the spacer and the continuous metal film at the back (Figure S5).

Due to the high stress developed in the SiO<sub>2</sub> case, presence of cracks in thin metal film is also observed in Figure 6d as indicated. On the other hand, no strong evidence of such permanent damage is observed in the AlN case (Figure 6c), even after the fourth cycle. Furthermore, the comparison between Figure 6c and d shows large deformation of the pattern in the SiO<sub>2</sub> case.

**Asymmetric Structure Analysis.** With such effect in mind, we further investigate into a set of asymmetric nanostructures (Figure 7e–i) with nanogap as small as 200 nm, where the stress effect should be relatively higher due to the asymmetry.

Such asymmetric nanostructure is potentially useful to achieve polarization tunability at high temperature. As shown in Figure

7a, strong polarization tunability can be indeed achieved at room temperature (before annealing) on SiO<sub>2</sub> platform, which can be interpreted with the help of polarization-dependent, resonant electric field distributions in Figure 7c,d. However, the tunability completely disappears (Figure 7b) when the SiO<sub>2</sub> device is annealed at 400 °C for 5 min. A careful investigation into the shape of the corresponding pattern further reveals its strong geometric deformation where the nanorod is touching the split ring, which were separated from each other by 200 nm otherwise. Similar type of shape deformation is consistently observed when the nanorod is gradually shifted downward with an offset (Figure 7k–n). We ascribe the geometric change observed in the SiO<sub>2</sub> case mainly to the reflow of the thin oxide layer under extreme thermal stress. For the cross wire nanostructure, the effect is found to deform the shape without much breaking the symmetry. However, for the axis asymmetric geometries, the effect is found to establish a conductive coupling between the nanostructures and, thereby, affect their resonance properties drastically (Figure 7b). Again, the AlN platform with minimum thermal stress is found to be robust against high temperature annealing even when the pattern shape is axis asymmetric and consists of nanogap (Figure 7e–i). Therefore, the proposed platform enables high temperature polarization tuning in coupled nanostructures for advanced mid-IR applications.

**Accumulated Stress Effect on AlN Film.** Nevertheless, we observe certain effects of accumulated stress in AlN device over multiple cycles as also indicated in Figure 5 before. The comparison of Raman spectra of AlN thin film on Mo collected before and after annealing (4th cycle) indeed show the effect of

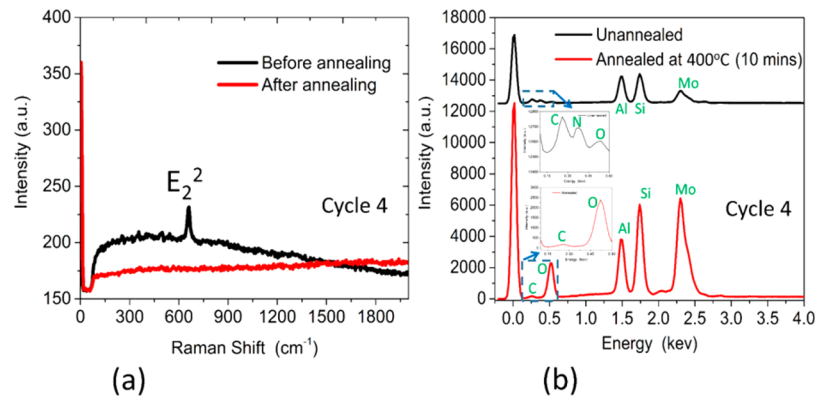


**Figure 8.** (a) Comparison of Raman spectra between fresh and annealed (4th cycle) AlN film on Mo reflector. The  $E_2^2$  peak indicates the crystalline nature of the AlN film. (b) SEM-EDS analysis of the effect of annealing (4th cycle) on AlN film on Mo reflector. The unannealed spectrum is vertically shifted for the purpose of clarity.

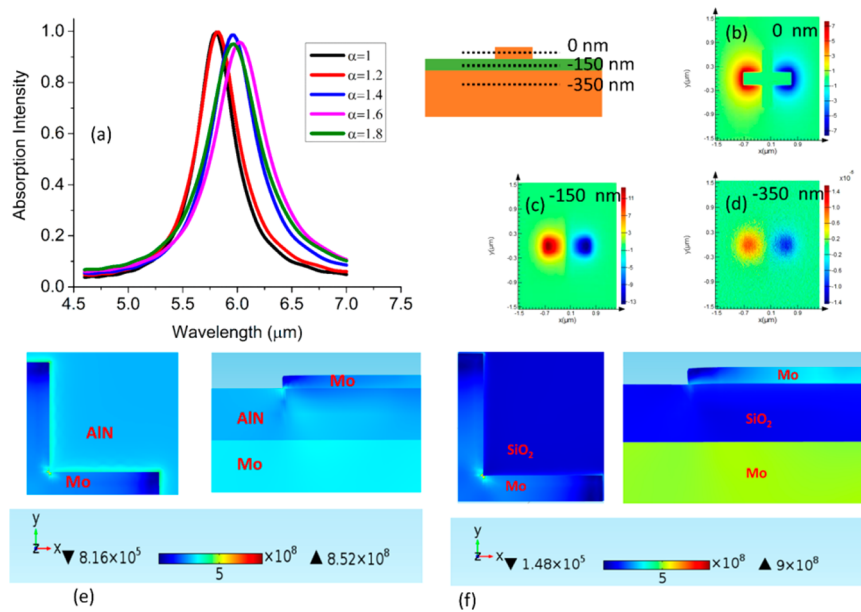


**Figure 9.** (a) Effect of increasing metal damping factor ( $\alpha$ ) on absorption spectrum. H-field distribution at (b) 0 nm plane, (c)  $-150$  nm plane, and (d)  $-350$  nm plane. (e) Von Mises stress distribution in Mo–AlN–Mo configuration (left,  $xy$  plane through the pattern; right,  $xz$  plane (cross section of the geometry) through the center of the pattern). (f) Von Mises distribution in Mo–SiO<sub>2</sub>–Mo configuration (left,  $xy$  plane through the pattern; right,  $xz$  plane (cross section of the geometry) through the center of the pattern).

the accumulated stress on the crystalline nature of AlN thin film. Besides, the SEM-EDS peak of nitrogen could not be detected in Figure 8b when the sample is annealed at 400 °C for four cycles. The material characterization results are indicative of the accumulated stress effect on the AlN thin film under repeated cycles of heating.

**Modeling of Reversible Intensity Change and Wavelength Shift.** We further deploy the modified Drude model of metal permittivity, which is defined as below to explain the reversible intensity change and wavelength shift:<sup>16,46</sup>

$$\hat{\epsilon} = 1 - \frac{\omega_p^2}{\omega^2 + i\alpha\Gamma\omega} \quad (5)$$

Here,  $\omega_p$  is the plasma frequency,  $\Gamma$  is the Drude damping parameter, and  $\alpha$  is the factor to quantify the increase in  $\Gamma$  due to the increased electron–electron scattering and electron–phonon scattering as the temperature is increased. However, the analysis does not take into account the arbitrary modification

of metal permittivity by the surface stress being related to the change of the lattice constant in thin film case.<sup>46</sup> Therefore, the effect of accumulated stress on the metal permittivity is ignored in this simulation. Nevertheless, the parameter  $\alpha$  can be fitted accordingly to model the temperature-dependent resistive part of the equivalent circuit for metamaterial absorber geometry.<sup>48</sup>

Figure 9a shows the simulated results for different values of  $\alpha$ . As expected on the premise of experimental results, the absorption intensity keeps dropping as the damping factor increases. Besides, the wavelength red shift also builds up similarly to the experiment as we increase  $\alpha$ . However, at some point ( $\alpha = 1.8$ ), the spectrum is found to blue shift. We attribute the overall permittivity-dependent shift to the complex interaction between the dipolar resonance of the metal pattern and its near-field coupling of the image dipole in the continuous back metal.<sup>49</sup> Temperature dependence of such interaction can be explored further in future. As a whole, we identify that the reversible nature of the resonance spectrum in low stress platform is directly related to the temperature dependence of the

metal permittivity. As Figure 4b shows, such a relationship is strongly violated when the platform is under high stress. We also simulate the Von Mises stress by assuming a heat stage touching the substrate. As shown in Figure 9b, the bottom metal plate is under relatively higher stress causing the interfacial damage, the predominant mechanism for breaking down the SiO<sub>2</sub> device.

**Temporal Measurement.** We consider the proposed Mo–AlN–Mo platform for fast thermal response, narrowband metamaterial absorber. Low response time is required for rapid feature detection in thermal imaging and high light power-to-temperature sensitivity. One approach for obtaining fast response is to reduce the thermal capacity of the structure by having subwavelength thickness which has its own process limitation and design challenge. Another viable approach could be increasing the thermal conductivity of the structure by choosing the appropriate material. The time-dependent modeling of reflection intensity ( $R$ ) based on the principle of transient heat conduction can be explained by the following sets of equation,

$$\frac{R(t) - R_i}{R_i - R_\alpha} = \exp(-bt) \quad (6)$$

$$b = \frac{hA}{\rho VC_p} \quad (7)$$

$$\tau_t = \frac{1}{b} \quad (8)$$

Here,  $R_i$  and  $R_\alpha$  are the reflection intensity at room temperature (25 °C) and final temperature (400 °C), respectively.  $\rho$ ,  $C_p$ , and  $h$  are the density, heat capacity, and thermal conductivity of the material, respectively.

We assume that the absolute value of reflection intensity at a given instant ( $t$ ) is directly proportional to the instantaneous temperature of the system. In this work, we propose AlN as the CMOS compatible solution for improving the response time of the metamaterial absorber structure. In Table 3, we provide a

**Table 3. Comparison of Time Constant Parameters between AlN and SiO<sub>2</sub>**

parameter	AlN	SiO <sub>2</sub>
$C_p$ (J/kg·K)	740	680
$\rho$ (g/cm <sup>3</sup> )	3.26	2.65
$h$ (W/m·k)	285	1.4

comparison of the time constant parameters between AlN and SiO<sub>2</sub>. Based on it, the bulk time constant ( $\tau_t$ ) in AlN thin film can be  $\sim 152\times$  less than in SiO<sub>2</sub> thin film. Based on the lumped parameter analysis of the multilayered structure in the presence of 500  $\mu\text{m}$  silicon substrate, its calculated to be  $27\times$  less, while all the geometrical parameters are kept identical.

**Prolonged Heating Effect.** For temporal measurement, we fix the temperature of the heat stage at 400 °C, which quickly ramps up to the final temperature in 1.66 min at a rate of 3.75 °C/s (Figure S6) and extract the minimum value from the instantaneous reflection data acquired by the time-resolved FTIR spectroscopy. The time difference between each measurement is 13 s. We capture the time dynamics of stress development in terms of both intensity change and resonance shift for about 23 min. The study under prolonged heating condition will be useful for assessing the device's thermal stability as an emitter. Figure 10 shows the temporal measurements that possess an exponential growth characteristics. The steep region of the growth curve corresponds to the response until the heat stage reaches saturation at 100 s. We fit the experimental data into two-term exponential model while accounting for the initial value of reflection and the linear like behavior after certain duration (200 s). As observed, the time constant factor ( $B$ ) of the positive exponent is  $15\times$  smaller in AlN device, implying  $15\times$  less rapid change than the SiO<sub>2</sub> device. In other words, the rate of degradation in the SiO<sub>2</sub> case due to the accumulating stress under prolonged condition is much higher than in the AlN case. We attribute the relatively higher robustness of the AlN platform to its low thermal stress configuration. Note that, here the heat stage temperature reaches stability within  $\sim 100$  s and any further change in intensity is mainly due to the stress-induced permittivity change and interfacial damage. We observe a saturation behavior of this change in the case of AlN device.

We further investigate into the time dynamics in Figure 11 for different geometries and observe identical behavior on both the platforms. Note that the growth curves for the SiO<sub>2</sub> devices fit very well into straight lines (dashed red) beyond 200 s, implying fast degradation over prolonged heating. We attempt to fit the linear portions of the spectra by bisquare polynomial of order 1 to explore the differences further. Within the range (600–1400 s), the SiO<sub>2</sub> devices show higher linearity, as expected with a fitness coefficient of 0.986. The slope of the fitting is always found to be less in AlN devices than that in the SiO<sub>2</sub> devices and reaches a minimum of  $2.4e-6$  under near-perfect absorption conditions. Ignoring the length effect on time constant, this implies  $25\times$  more robust performance of the AlN device as an

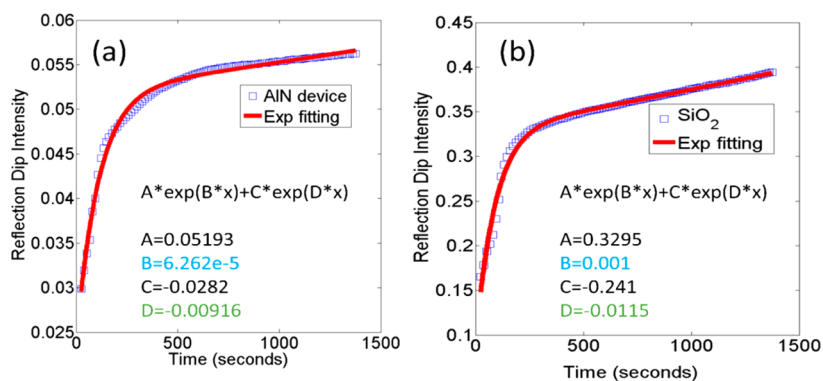


**Figure 10.** Exponential development of reflection dip intensity with time when the heat stage is programmed at 400 °C: (a) AlN device; (b) SiO<sub>2</sub> device. Spacer thickness is fixed at 200 nm in both cases, and the cross wire geometry is considered.

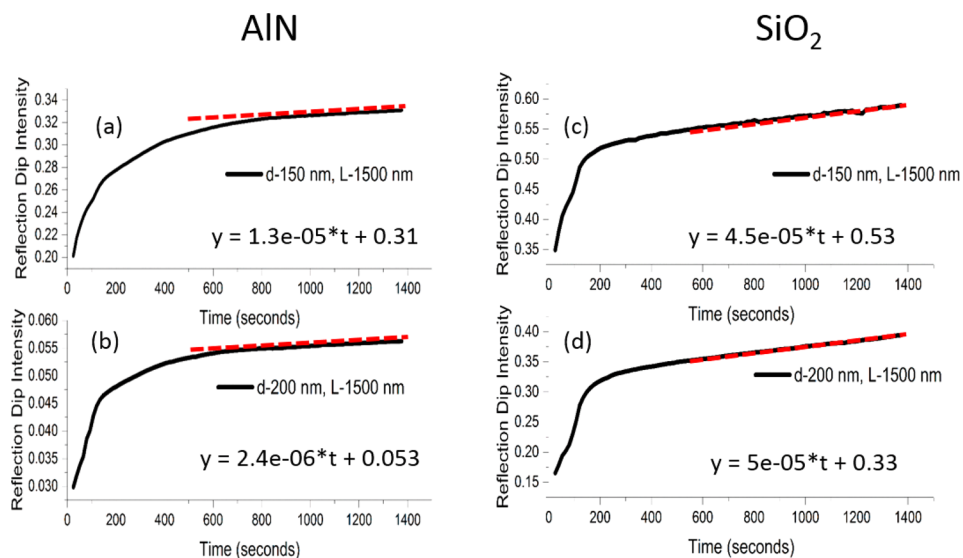


**Figure 11.** (a) Temporal measurement of the mid-IR absorber structures. Time response of the reflection dip intensity: (a) AlN structure ( $d$ , 150 nm;  $L$ , 1500 nm). (b) AlN structure ( $d$ , 200 nm;  $L$ , 1500 nm). (c) SiO<sub>2</sub> structure ( $d$ , 150 nm;  $L$ , 1500 nm). (d) SiO<sub>2</sub> structure ( $d$ , 200 nm;  $L$ , 1500 nm).

emitter operating at 400 °C as compared to the SiO<sub>2</sub> device with identical spacer thickness. In the case of full-scale linear fitting of the data beyond 200 s, we observe 10× more robust performance of the AlN device (Figures S7 and S8). In this case, the fitness coefficient is 0.9436. Again, comparison between Figure 11a and b shows that the near-perfect absorption condition of the AlN device (Figure 11b) can offer at least 6× less intensity variation across the whole time range.

Later, we focus on the resonance wavelength shift with time. As shown in Figure 12, we observe a stair case development of the resonance red shift as the sample temperature is fixed at 400 °C for 1400 s (~23 min). The envelopes of the time-dependent development can again be fitted into two-term exponential model (Figures S9 and S10). In this case, we attribute the overall shift to the permittivity change of the metal layers with time. However, due to the stress accumulating within the system with time, the lattice constant is also affected. The stair case nature of the wavelength shift is possibly arose by such quantized change in metal permittivity due to the lattice change in time. Interestingly, for the low-stress AlN platform, we always observe a continuous growth of the wavelength shift with a positive slope. However, in the case of high-stress SiO<sub>2</sub> platform, such behavior is not preserved across the entire range.

Our observation is also found to be consistent in Figure 12a–d, regardless of the device geometrical parameters.

To further investigate into the quantized nature of the shift, we provide the results on the SiO<sub>2</sub> platform in Figure 12e and f, captured at 4 and 2 cm<sup>-1</sup>, respectively. As observed, the quantized shift is still preserved in the temporal measurements. At higher resolution, we also notice certain spikes that may be attributed to the stress relaxation within the system occurring for a short time. The wavelength red-shift observed under dynamic heating in Figure 12 and after heating in Figure 5 strongly indicates the role of stress-induced lattice dilation/contraction of metal.<sup>46</sup> In general, lattice dilation would decrease electron

density in metal and, hence, the plasma frequency  $\omega_p^2 = \frac{n_e e^2}{m \times \epsilon_0}$ . Decrease of plasma frequency will further decrease the dielectric contrast under Drude model approximation causing red shift in metamaterial absorber configuration. For further verification, we

consider a unique case of Mo–AlN–Mo platform with a 100 nm compressive SiO<sub>2</sub> layer on top shown in Figure 12g,h. Unlike the previous cases, here we observe red-shift only for a short duration, followed by a pronounced blue-shift. Again, we observe a quantized shift at reasonably high resolution scanning (2 cm<sup>-1</sup>). We propose that, the oxide top layer can exert compressive stress causing lattice contraction, and thereby increase the plasma frequency and blue-shift the energy of the resonant absorber. The reflection intensity, however, maintains an ideal transient dynamics in Figure 12h, as discussed before. The focal plane array measurements in Figure 13a,b ensure the good uniformity of the temperature driven effect across the whole array. Furthermore, the comparison in Figure 13c clearly indicates the role of compressive stress behind the blue-shift of the resonance. We also confirm the stability of the measurement setup at high resolution by scanning across the spectra of AlN–Mo stack for maximum reflection point (Figure S11). Unlike the absorber case, we observe a decrease of reflection intensity which is directly in agreement with the temperature dependence of Drude damping. Moreover, the rate of decrease in this case is much smaller than the rate of increase in the absorber case due to the absence of any resonant interaction. Our study opens up a new avenue for engineering the stress induced resonance shift for the ultimate stabilization of low stress Mo–AlN–Mo metamaterial absorber. Our preliminary results confirm that such shift occurs in a quantized nature. Finally, we assume the simultaneous function of temperature-dependent damping and stress-dependent plasma frequency of metal behind the overall time-dependent profile under prolonged heating condition where the damping governs the exponential development and the plasma frequency governs the quantized behavior. Additional materials research might be needed in the future to explore the mechanism in depth.

**Surface Enhanced Infrared Absorption Spectroscopy on the platform.** Here, we explore the feasibility of the proposed platform as a CMOS compatible alternative to purely gold-based approach for surface enhanced infrared absorption spectroscopy (SEIRA) of chemicals and gases. One unique advantage of the low thermal stress platform is its viability for low form factor integration into the sensing architecture as a narrow band blackbody emitter. Together with the nonlinearity of AlN,

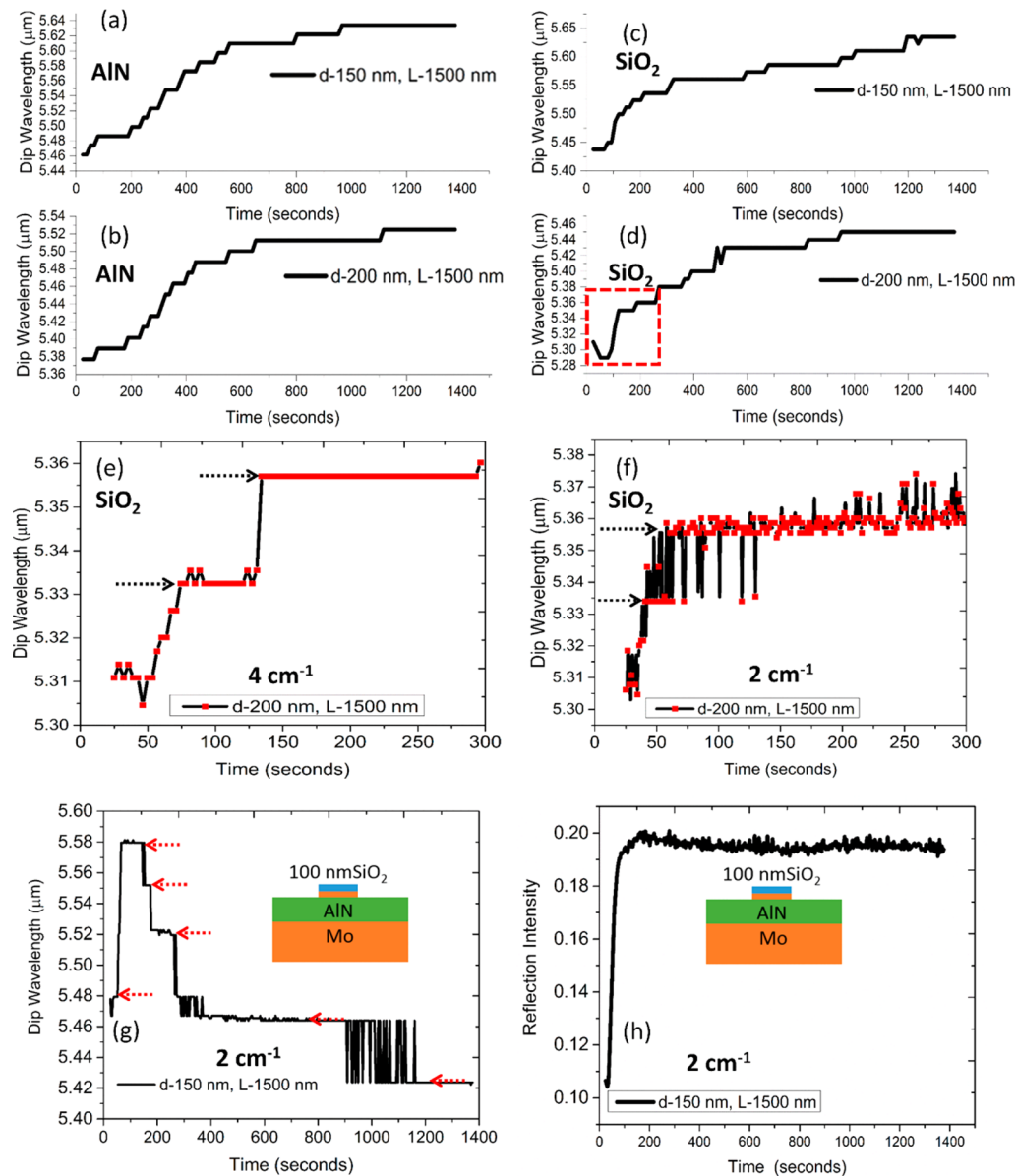


**Figure 12.** (a) Temporal measurement of the mid-IR absorber structures. Time response of the dip wavelength: (a) AlN structure ( $d$ , 150 nm;  $L$ , 1500 nm). (b) AlN structure ( $d$ , 200 nm;  $L$ , 1500 nm). (c) SiO<sub>2</sub> structure ( $d$ , 150 nm;  $L$ , 1500 nm). (d) SiO<sub>2</sub> structure ( $d$ , 200 nm;  $L$ , 1500 nm). Temporal measurement of wavelength shift within the indicated region in (d) at (e) 4 cm<sup>-1</sup> resolution and at (f) 2 cm<sup>-1</sup> resolution. Temporal measurement in the presence of compressive stress layer at 2 cm<sup>-1</sup> resolution (g) wavelength shift and (h) intensity modulation.

the mid-IR to visible light upconversion mechanism also becomes readily available on chip. In the presence of chemical specific weak vibrational resonance (“quasi dark mode”), the absorption resonance (“bright mode”) of the metamaterial can strongly interact, depending on the geometric parameters and constitute a coupled system with large dispersion. The linear susceptibility ( $\chi$ ) of the coupled system can be expressed as<sup>16</sup>

$$\chi = \frac{K}{A^2 B} \left( \frac{A(B+1)\Omega^2 + A^2(\omega^2 - \omega_d^2) + B(\omega^2 - \omega_b^2)}{\Omega^4 - (\omega^2 - \omega_b^2 + i\omega\Gamma)(\omega^2 - \omega_d^2 + i\omega\gamma)} + i\omega \frac{A^2\gamma + B\Gamma}{\Omega^4 - (\omega^2 - \omega_b^2 + i\omega\Gamma)(\omega^2 - \omega_d^2 + i\omega\gamma)} \right) \quad (10)$$

Here, ( $\gamma$ ,  $\Gamma$ ) and ( $\omega_d$ ,  $\omega_b$ ) are the loss rate (line width) and resonance angular frequencies of the “quasi dark mode” and

“bright mode”, respectively.  $\Omega$  is the coupling strength and  $A$  and  $B$  are the dimensionless constants dictating the relative coupling of incoming radiation with the “bright mode” and “quasi dark mode”, respectively, and  $K$  is the amplitude offset. However, the proposed platform may still lack the required biocompatibility and surface functionalizability for a wide range of biological samples. Often gold is used to preserve such prerequisite properties for mid-IR sensing.<sup>50</sup> On the other hand, metallic oxide surface such as Al<sub>2</sub>O<sub>3</sub> is routinely used for culturing self-assembled monolayers (SAM).<sup>51</sup> The thin (10 nm) ALD coating of Al<sub>2</sub>O<sub>3</sub> can be obtained on demand within the existing CMOS process flow. Additionally, we propose to coat the absorber structure with a very thin layer of gold (5 nm) by electron beam evaporation to circumvent the biocompatible issue. The techniques can be easily implemented in a batch process while providing a biocompatible surface for the chemical reactions. The modified geometries are shown at the insets of Figure 14a. As the gold coating introduces

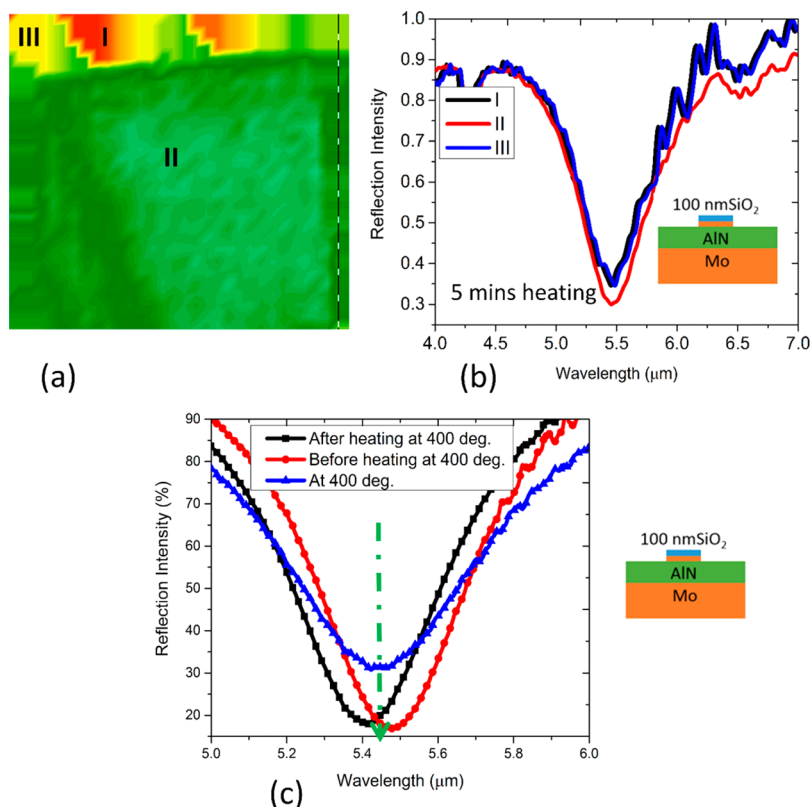


**Figure 13.** (a) Focal plane array image ( $100 \times 100 \mu\text{m}^2$ ) collected under continuous heating at  $400^\circ\text{C}$  for 5 min. (b) Collected spectra at three distinct regions showing uniformity of the temperature driven effect across the area. (c) Wavelength shift and intensity modulation with respect to the original device observed at two different instances. The net residual stress can be comprehended from the blue-shifted black spectrum collected as the sample cools down.

additional loss in the system, we indeed observe a broadening of the absorption resonance in Figure 14a. Furthermore, additional reflection from the thin gold layer increases the value of the reflection dip and thereby reduces the overall absorption. However, the geometric scalability of the modified platform is still found to be valid as the length of the nanorod is increased from 1.5 to 2.4  $\mu\text{m}$  in Figure 14b. On the other hand, the  $\text{Al}_2\text{O}_3$  coating is found to have a negligible effect on the device. Later, we investigate into the coupling behavior of the two modified platforms: (i) gold (Au) covered and (ii) 10 nm ALD  $\text{Al}_2\text{O}_3$  coated absorber by functionalizing with a 50 nm silk fibroin film possessing two distinct amide peaks. As observed in Figure 14c,d, strong geometry-dependent coupling into the peaks is observed in both cases. The coupling coefficient ( $\Omega$ ) is supposedly to be at maximum when the geometric parameters are optimized for the detection of the amide peaks (C4 in  $\text{Al}_2\text{O}_3$  case and C3 in gold case). We further plot the difference signals ( $R_{\text{bare}} - R_{\text{coated}}$ ) in Figure 14e,f. The transition of the difference signal at the onset of the first amide peak is noticeable in both cases. The results are strongly suggestive of the sensitivity of the CMOS compatible absorber platform even when it is modified to support a wide range of chemical kinetics to be monitored by surface enhanced infrared absorption spectroscopy.

## CONCLUSION

In conclusion, we have demonstrated a versatile CMOS platform of refractory metamaterial absorber with low thermal stress and better durability for narrowband applications, fast thermal response, and potential for surface enhanced infrared absorption spectroscopy on a large scale. Our static and time-dependent

analysis clearly shows the robustness of the platform under prolonged heating over multiple cycles. We particularly address the design challenges of TiN-based CMOS compatible platform for narrowband refractory applications in the mid- to far-IR spectrum in this regard. We demonstrate excellent geometric scalability of the platform by leveraging the broadband transparency of AlN, which also benefits from its nonlinear property and can possibly harness its piezoelectric property for actuation in future. Besides, the high oxidation temperature and chemical stability of Mo have made it possible to operate in the ambient condition.<sup>52</sup> It is expected that the working temperature of the device platform can be increased further without incurring any critical damage. Based on the analytical calculation, the proposed platform is also expected to achieve rapid response time while relaxing the rigid limit of the active device thickness, which therefore reduces the process challenge and design complexity. Although the demonstrated SEIRA sensitivity may be still below that which is obtainable with state-of-the-art gold devices, the platform being CMOS compatible and thus easily integrable with readout electronics, can eventually be used to construct intelligent sensing networks with a large number of sensing nodes at a tangibly lower cost. Therefore, the developed platform is a promising avenue for the realization of CMOS compatible mid- to far-IR devices aimed at highly integrated chemical specific molecular sensing, thermal imaging, and thermophotovoltaic energy harvesting.

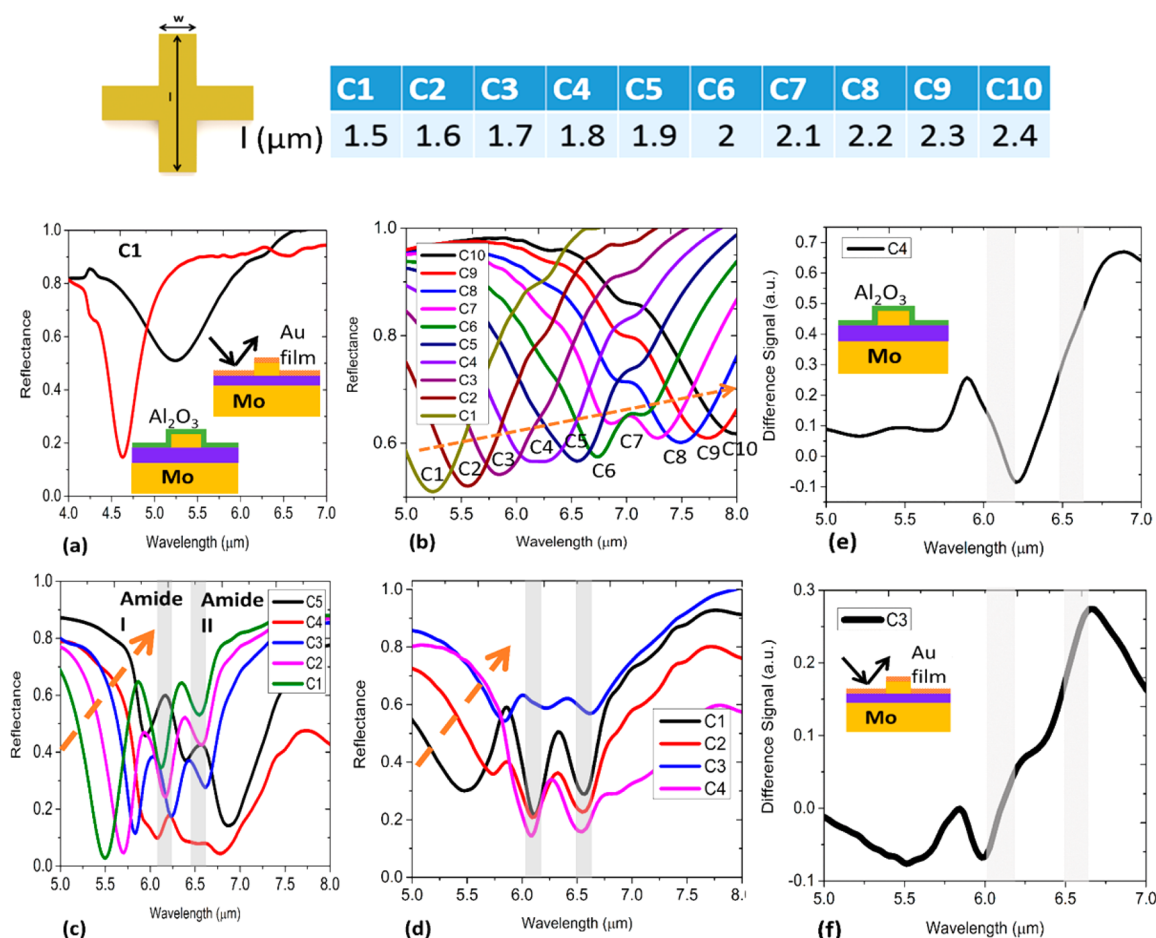


**Figure 14.** (a) Comparison of resonance characteristics between the 5 nm Au covered and 10 nm  $\text{Al}_2\text{O}_3$ -coated CMOS absorber. Inset: Relevant geometries. Additional reflection off the 5 nm Au film is marked by the black arrow. (b) Length variation effect of the Au covered absorber structure. The dashed arrow indicates the resonance shift observed. (c) Geometry-dependent coupling into the amide bands of 100 nm Si film as the length of the as fabricated absorber coated with 10 nm ALD  $\text{Al}_2\text{O}_3$  film is varied. (d) Geometry-dependent coupling into amide bands as the length of the Au covered absorber is varied. The dashed arrows indicate the shift of resonance as the length of the pattern increases. (e) Difference signal ( $R_{\text{bare}} - R_{\text{coated}}$ ) when  $\text{Al}_2\text{O}_3$  coating is used. (f) Difference signal ( $R_{\text{bare}} - R_{\text{coated}}$ ) when gold coating is used.

## ■ ASSOCIATED CONTENT

### Supporting Information

The Supporting Information is available free of charge on the ACS Publications website at DOI: 10.1021/acsp Photonics.6b00672.

Discussion on additional experimental results on the comparison between Mo and TiN and time-dependent characteristics under prolonged heating condition (PDF).

## ■ AUTHOR INFORMATION

### Corresponding Author

\*E-mail: elelc@nus.edu.sg.

### ORCID

Chengkuo Lee: 0000-0002-8886-3649

### Notes

The authors declare no competing financial interest.

## ■ ACKNOWLEDGMENTS

The authors acknowledge the financial support from the Research Grants of MOE2012-T2-2-154 “Monolithic integrated Si/AlN nanophotonics platform for optical NEMS and OEICs” (WBS: R-263-000-A59-112) at NUS, Singapore; NRF-CRP15-

2015-02 “Piezoelectric Photonics Using CMOS Compatible AlN Technology for Enabling The Next Generation Photonics ICs and Nanosensors” (WBS: R-263000C24281) at NUS, Singapore; and the partial support by National Natural Science Foundation of China under Grant No. 61474078 at NUS (Suzhou) Research Institute, Suzhou, China, and Grant No. 61674104 at Shanghai Jiao Tong University, Shanghai, China.

## ■ REFERENCES

- (1) Caldarola, M.; Albella, P.; Cortés, E.; Rahmani, M.; Roschuk, T.; Grinblat, G.; Oulton, R. F.; Bragas, A. V.; Maier, S. A. Non-Plasmonic Nanoantennas for Surface Enhanced Spectroscopies with Ultra-Low Heat Conversion. *Nat. Commun.* **2015**, *6*, 7915.
- (2) Esfandyarpour, M.; Garnett, E. C.; Cui, Y.; McGehee, M. D.; Brongersma, M. L. Metamaterial Mirrors in Optoelectronic Devices. *Nat. Nanotechnol.* **2014**, *9*, 542–547.
- (3) Lenert, A.; Bierman, D. M.; Nam, Y.; Chan, W. R.; Celanovic, I.; Soljacic, M.; Wang, E. N. A Nanophotonic Solar Thermophotovoltaic Device. *Nat. Nanotechnol.* **2014**, *9*, 126–130.
- (4) Dregely, D.; Lindfors, K.; Lippitz, M.; Engheta, N.; Totzeck, M.; Giessen, H. Imaging and Steering an Optical Wireless Nanoantenna Link. *Nat. Commun.* **2014**, *5*, 4354.
- (5) Kumar, K.; Duan, H.; Hegde, R. S.; Koh, S. C. W.; Wei, J. N.; Yang, J. K. W. Printing Colour at the Optical Diffraction Limit. *Nat. Nanotechnol.* **2012**, *7*, 557–561.

- (6) Della Giovampaola, C.; Engheta, N. Digital Metamaterials. *Nat. Mater.* **2014**, *13*, 1115–1121.
- (7) Bidault, S.; Devilez, A.; Ghenuche, P.; Stout, B.; Bonod, N.; Wenger, J. Competition between Förster Resonance Energy Transfer and Donor Photodynamics in Plasmonic Dimer Nanoantennas. *ACS Photonics* **2016**, *3*, 895.
- (8) Zhu, W.; Crozier, K. B. Quantum Mechanical Limit to Plasmonic Enhancement as Observed by Surface-Enhanced Raman Scattering. *Nat. Commun.* **2014**, *5*, 5228.
- (9) Biosensing, a; Cao, C.; Zhang, J.; Wen, X.; Dodson, S. L.; Dao, N. T.; Wong, L. M. Metamaterials-Based Label-Free Nanosensor for Conformation and Affinity Biosensing. *ACS Nano* **2013**, *7*, 7583–7591.
- (10) Liu, Y.; Park, Y.; Lee, S. E. Thermo-Responsive Mechano-Optical Plasmonic Nano-Antenna. *Appl. Phys. Lett.* **2016**, *109*, 013109.
- (11) Singh, R.; Zheludev, N. Materials: Superconductor Photonics. *Nat. Photonics* **2014**, *8*, 679–680.
- (12) Cong, L.; Xu, N.; Chowdhury, D. R.; Manjappa, M.; Rockstuhl, C.; Zhang, W.; Singh, R. Nonradiative and Radiative Resonances in Coupled Metamolecules. *Adv. Opt. Mater.* **2016**, *4*, 252–258.
- (13) Yi, F.; Ren, M.; Reed, J. C.; Zhu, H.; Hou, J.; Naylor, C. H.; Johnson, A. T. C.; Agarwal, R.; Cubukcu, E. Optomechanical Enhancement of Doubly Resonant 2D Optical Nonlinearity. *Nano Lett.* **2016**, *16*, 1631–1636.
- (14) Son, J. H.; Cho, B.; Hong, S.; Lee, S. H.; Hoxha, O.; Haack, A. J.; Lee, L. P. Ultrafast Photonic PCR. *Light: Sci. Appl.* **2015**, *4*, e280.
- (15) Hasan, D.; Ho, C. P.; Pitchappa, P.; Lee, C. Dipolar Resonance Enhancement and Magnetic Resonance in Cross-Coupled Bow-Tie Nanoantenna Array by Plasmonic Cavity. *ACS Photonics* **2015**, *2*, 890–898.
- (16) Hasan, D.; Ho, C. P.; Pitchappa, P.; Yang, B.; Yang, C.; Lee, C. Thermoplasmonic Study of a Triple Band Optical Nanoantenna Strongly Coupled to Mid IR Molecular Mode. *Sci. Rep.* **2016**, *6*, 22227.
- (17) Hasan, D.; Ho, C. P.; Lee, C. Thermally Tunable Absorption-Induced Transparency by a Quasi 3D Bow-Tie Nanostructure for Nonplasmonic and Volumetric Refractive Index Sensing at Mid-IR. *Adv. Opt. Mater.* **2016**, *4*, 943–952.
- (18) Xu, X.; Hasan, D.; Wang, L.; Chakravarty, S.; Chen, R. T.; Fan, D. L.; Wang, A. X. Guided-Mode-Resonance-Coupled Plasmonic-Active SiO<sub>2</sub> Nanotubes for Surface Enhanced Raman Spectroscopy. *Appl. Phys. Lett.* **2012**, *100*, 191114.
- (19) Xu, X.; Li, H.; Hasan, D.; Ruoff, R. S.; Wang, A. X.; Fan, D. L. Near-Field Enhanced Plasmonic-Magnetic Bifunctional Nanotubes for Single Cell Bioanalysis. *Adv. Funct. Mater.* **2013**, *23*, 4332–4338.
- (20) Hasan, D.; Alam, M. S. Ultra-Broadband Confinement in Deep Sub-Wavelength Air Hole of a Suspended Core Fiber. *J. Lightwave Technol.* **2014**, *32*, 1434–1441.
- (21) Ren, F.; Campbell, J.; Hasan, D.; Wang, X.; Rorrer, G. L.; Wang, A. X. Bio-Inspired Plasmonic Sensors by Diatom Frustules. *CLEO: 2013*; OSA: Washington, D.C., 2013; p CTh3L4.
- (22) Hasan, D.; Wang, J.; Lee, C. Fractal Engineered Voids for Non-Resonant Nano-Plasmonic Detection of Weak Molecular Fingerprint at Mid IR. *2016 IEEE 29th International Conference on Micro Electro Mechanical Systems (MEMS)*; IEEE **2016**, 234–237.
- (23) Hasan, D.; Chong, P.; Ho, C. P.; Pitchappa, P.; Chengkuo Lee, C. Plasmonic Cavity Assisted Dipolar Resonance Enhancement and Optical Magnetism at Mid IR. *2015 International Conference on Optical MEMS and Nanophotonics (OMN)*; IEEE, 2015; pp 1–2.
- (24) Kuzyk, A.; Schreiber, R.; Zhang, H.; Govorov, A. O.; Liedl, T.; Liu, N. Reconfigurable 3D Plasmonic Metamolecules. *Nat. Mater.* **2014**, *13*, 862–866.
- (25) Chanda, D.; Shigeta, K.; Gupta, S.; Cain, T.; Carlson, A.; Mihi, A.; Baca, A. J.; Bogart, G. R.; Braun, P.; Rogers, J. A. Large-Area Flexible 3D Optical Negative Index Metamaterial Formed by Nanotransfer Printing. *Nat. Nanotechnol.* **2011**, *6*, 402–407.
- (26) De Angelis, F.; Malerba, M.; Patrini, M.; Miele, E.; Das, G.; Toma, A.; Zaccaria, R. P.; Di Fabrizio, E. 3D Hollow Nanostructures as Building Blocks for Multifunctional Plasmonics. *Nano Lett.* **2013**, *13*, 3553–3558.
- (27) Chong Pei Ho, C. P.; Pitchappa, P.; Kropelnicki, P.; Jian Wang, J.; Yuandong Gu, Y.; Chengkuo Lee, C. Development of Polycrystalline Silicon Based Photonic Crystal Membrane for Mid-Infrared Applications. *IEEE J. Sel. Top. Quantum Electron.* **2014**, *20*, 94–100.
- (28) Ho, C. P.; Pitchappa, P.; Kropelnicki, P.; Wang, J.; Cai, H.; Gu, Y.; Lee, C. Two-Dimensional Photonic-Crystal-Based Fabry–Perot Etalon. *Opt. Lett.* **2015**, *40*, 2743.
- (29) Pitchappa, P.; Pei, H. C.; Kropelnicki, P.; Singh, N.; Kwong, D.-L.; Lee, C. Micro-Electro-Mechanically Switchable near Infrared Complementary Metamaterial Absorber. *Appl. Phys. Lett.* **2014**, *104*, 201114.
- (30) Pitchappa, P.; Manjappa, M.; Ho, C. P.; Singh, R.; Singh, N.; Lee, C. Metamaterials: Active Control of Electromagnetically Induced Transparency Analog in Terahertz MEMS Metamaterial (Advanced Optical Materials 4/2016). *Adv. Opt. Mater.* **2016**, *4*, 540–540.
- (31) Pitchappa, P.; Ho, C. P.; Cong, L.; Singh, R.; Singh, N.; Lee, C. Reconfigurable Digital Metamaterial for Dynamic Switching of Terahertz Anisotropy. *Adv. Opt. Mater.* **2016**, *4*, 391–398.
- (32) Li, J. L.; Day, D.; Gu, M. Ultra-Low Energy Threshold for Cancer Photothermal Therapy Using Transferrin-Conjugated Gold Nanorods. *Adv. Mater.* **2008**, *20*, 3866–3871.
- (33) Zhou, N.; Xu, X.; Hammack, A. T.; Stipe, B. C.; Gao, K.; Scholz, W.; Gage, E. C. Plasmonic near-Field Transducer for Heat-Assisted Magnetic Recording. *Nanophotonics* **2014**, *3*, 141–155.
- (34) Zhou, Z.; Chen, Q.; Bermel, P. Prospects for High-Performance Thermophotovoltaic Conversion Efficiencies Exceeding the Shockley–Queisser Limit. *Energy Convers. Manage.* **2015**, *97*, 63–69.
- (35) Bhattacharya, A.; Bhattacharyya, S.; Ghosh, S.; Chaurasiya, D.; Vaibhav Srivastava, K. An Ultrathin Penta-Band Polarization-Insensitive Compact Metamaterial Absorber for Airborne Radar Applications. *Microw. Opt. Technol. Lett.* **2015**, *57* (11), 2519–2524.
- (36) Guler, U.; Shalae, V. M.; Boltasseva, A. Nanoparticle Plasmonics: Going Practical with Transition Metal Nitrides. *Mater. Today* **2015**, *18*, 227–237.
- (37) Shemelya, C.; DeMeo, D.; Latham, N. P.; Wu, X.; Bingham, C.; Padilla, W.; Vandervelde, T. E. Stable High Temperature Metamaterial Emitters for Thermophotovoltaic Applications. *Appl. Phys. Lett.* **2014**, *104*, 201113.
- (38) Tagliabue, G.; Eghlidi, H.; Poulikakos, D. Rapid-Response Low Infrared Emission Broadband Ultrathin Plasmonic Light Absorber. *Sci. Rep.* **2014**, *4*, 7181.
- (39) Dayal, G.; Anantha Ramakrishna, S. Multipolar Localized Resonances for Multi-Band Metamaterial Perfect Absorbers. *J. Opt.* **2014**, *16* (9), 94016.
- (40) Miyazaki, H. T.; Kasaya, T.; Iwanaga, M.; Choi, B.; Sugimoto, Y.; Sakoda, K. Dual-Band Infrared Metasurface Thermal Emitter for CO<sub>2</sub> Sensing. *Appl. Phys. Lett.* **2014**, *105*, 121107.
- (41) Baldassarre, L.; Sakat, E.; Frigerio, J.; Samarelli, A.; Gallacher, K.; Calandrini, E.; Isella, G.; Paul, D. J.; Ortolani, M.; Biagioni, P. Mid infrared Plasmon-Enhanced Spectroscopy with Germanium Antennas on Silicon Substrates. *Nano Lett.* **2015**, *15*, 7225–7231.
- (42) Law, S.; Yu, L.; Rosenberg, A.; Wasserman, D. All-Semiconductor Plasmonic Nanoantennas for Infrared Sensing. *Nano Lett.* **2013**, *13*, 4569–4574.
- (43) Dam, J. S.; Tidemand-Lichtenberg, P.; Pedersen, C. Room-Temperature Mid-Infrared Single-Photon Spectral Imaging. *Nat. Photonics* **2012**, *6*, 788–793.
- (44) Guler, U.; Shalae, V. M.; Boltasseva, A. Nanoparticle Plasmonics: Going Practical with Transition Metal Nitrides. *Mater. Today* **2015**, *18*, 227–237.
- (45) Chen, H.-T. Interference Theory of Metamaterial Perfect Absorbers. *Opt. Express* **2012**, *20*, 7165.
- (46) Alabastris, A.; Tuccio, S.; Giugni, A.; Toma, A.; Liberale, C.; Das, G.; Angelis, F.; Fabrizio, E.; Zaccaria, R. Molding of Plasmonic Resonances in Metallic Nanostructures: Dependence of the Non-Linear Electric Permittivity on System Size and Temperature. *Materials* **2013**, *6*, 4879–4910.
- (47) Ordal, M. A.; Bell, R. J.; Alexander, R. W.; Long, L. L.; Querry, M. R. Optical Properties of Fourteen Metals in the Infrared and Far

Infrared: Al, Co, Cu, Au, Fe, Pb, Mo, Ni, Pd, Pt, Ag, Ti, V, and W. *Appl. Opt.* **1985**, *24*, 4493.

(48) Bhattacharyya, S.; Ghosh, S.; Srivastava, K. V. Equivalent Circuit Model of an Ultra-Thin Polarization-Independent Triple Band Metamaterial Absorber. *AIP Adv.* **2014**, *4* (9), 97127.

(49) Yu, B.; Woo, J.; Kong, M.; O'Carroll, D. M. Mode-Specific Study of Nanoparticle-Mediated Optical Interactions in an Absorber/metal Thin Film System. *Nanoscale* **2015**, *7*, 13196–13206.

(50) Newton, L.; Slater, T.; Clark, N.; Vijayaraghavan, A. Self Assembled Monolayers (SAMs) on Metallic Surfaces (Gold and Graphene) for Electronic Applications. *J. Mater. Chem. C* **2013**, *1*, 376–393.

(51) Jadhav, S. A. Self-Assembled Monolayers (SAMs) of Carboxylic Acids: An Overview. *Cent. Eur. J. Chem.* **2011**, *9*, 369–378.

(52) Park, J. H.; Han, S. E.; Nagpal, P.; Norris, D. J. Observation of Thermal Beaming from Tungsten and Molybdenum Bull's Eyes. *ACS Photonics* **2016**, *3*, 494–500.